Materials Advances

ROYAL SOCIETY OF CHEMISTRY

PAPER

View Article Online
View Journal

Cite this: DOI: 10.1039/d6ma00174b

Optoelectronic characterization and thermoelectric figure-of-merit optimization of newly synthesized spirothiadiazole–thienothiophene-based macroheterocyclic compounds

E. Kh. Shokr,[a] Souhaila S. Enaili,[b] Moumen S. Kamel,*[c] Sh. A. Elkot[a] and Ahmed M. El-Saghier[c]

This work describes the synthesis of some novel organic compounds, along with the evaluation of their optoelectronic characteristics and potential for thermoelectric applications. The newly synthesized spirothiadiazole–thienothiophene-based macroheterocyclic compounds were termed as **Kz1–Kz3**. The synthesis of compounds followed a green approach: the one-pot condensation of thienothiophene thiohydrazide with different ketones afforded macrocyclic spiroheterocycles in good yields. Using FT-IR and NMR spectroscopies and elemental analysis, the compounds' structures were confirmed. Thin-film optical studies revealed strong absorption and high transparency in UV-vis and NIR spectral ranges, respectively. Depending on the degree of conjugation, the energy gaps ranged from 2.99 to 3.26 eV with indirect allowed transitions. Dielectric and dispersion studies provided evidence of high refractive index and high polarizability, confirming their potential as optoelectronic devices. Thermoelectric studies demonstrated that the samples are n-type semiconductors with negative Seebeck coefficients and temperature-dependent conductivities. Among the synthesized compounds, the **Kz2** compound showed the best thermoelectric performance with a power factor (PF) of 366 μW m^{-1} K^{-2} and a zT of 0.78 at 493 K after annealing at 200 °C for 5 minutes. The preliminary outcomes of this work clearly demonstrated the potential of spirothiadiazole–thienothiophene frameworks for use in next-generation flexible, eco-friendly thermoelectric and optoelectronic applications.

Received 6th February 2026,
Accepted 18th April 2026

DOI: 10.1039/d6ma00174b

rsc.li/materials-advances

1. Introduction

The interest in green technology based on organic thermoelectric materials has arisen due to concerns over the exhaustion of traditional fossil fuel sources and the climate change impacts caused by these fuels.

Organic semiconductors have captivated researchers over the past few decades due to their extraordinary optical and electronic properties, solution processability, significant structural versatility, and use as low-cost electronic devices capable of bending.[1–5] Among the numerous classes of conjugated organic molecules, heterocyclic compounds with fused thiophene units are notable for their tunability and high charge carrier mobility. Organic semiconductors are quite promising materials with a wide range of applications in organic light-emitting diodes (OLEDs),[6] organic photovoltaic cells (OPVs)[7] and organic field-effect transistors (OFETs).[8] In the family of conjugated organic molecules, thienothiophene derivatives are particularly attractive building blocks owing to their extended conjugation and desirable electronic characteristics.

Fused-ring compounds condensed by two thiophene units are referred to as thienothiophenes. The two thiophene rings are connected *via* a shared bond within a fused framework, enabling partial planarity and limited π-conjugation. Planarity enables the compounds to exhibit efficient intermolecular stacking and charge carrier transport.[9,10] The rigid and planar backbone of thienothiophenes will minimize the torsional disorder while allowing improved thin-film crystallinity and providing forces for efficient π–π interactions–properties that are preferable for optoelectronic devices.[11–13] The excellent application of substituted functional groups at various positions is attractive for attaining tailored material properties that tune electronic conditions.

[a] *Physics Department, Faculty of Science, Sohag University, Sohag 82524, Egypt*
[b] *Pharmaceutical Chemistry Department, Faculty of Pharmacy, University of Zawia, Al Zawia 16418, Libya*
[c] *Chemistry Department, Faculty of Science, Sohag University, Sohag 82524, Egypt. E-mail: mim_chem2@yahoo.com*

In recent years, attention has been paid to the synthesis of new derivatives of thienothiophenes with multiple substituents to modify the energy levels, band gaps and solubility of thienothiophenes.[10,13,14] These substituents comprise electron-donating groups (EDGs) and electron-withdrawing groups (EWGs) to modify the electron-donating ability of thienothiophenes at the frontier molecular orbitals for fine-controlling absorption and emission properties as well as the ionization potentials and electron affinities.[14–17] This degree of molecular engineering can be important after the synthesis of thienothiophenes to consider compatibility with the device architecture or simply the other functional layers.

In addition to their optical properties, the electrical properties of thienothiophene-based materials are equally important for the incorporation of these materials into electronic devices. Charge carrier mobilities, conductivities, and stabilities indicate the usefulness of these materials as the active layers in OFETs and other devices.[18–20] There are excess design choices to enhance the charge transport properties by increasing the ordered molecular arrangements and decreasing the trap densities, such as increasing backbone planarity and side-chain engineering to promote molecular alignment or utilizing donor–acceptor systems to enhance interactions between ordered molecules.[21] Moreover, the thieno[3,2-*b*] thiophene motif has often been touted as the one on account of its high level of conjugation and natural planeness, and the thieno[2,3-*b*] thiophene motif provides an anti-delocalized electronic topology, wherein the spatial arrangement of sulfur atoms and the fusion of rings explicitly put a limit on delocalization. This controllable conjugation has been shown to be central in the control of optical band gaps, carrier densities and thermoelectric responsiveness in small-molecule organic semiconductors.

Thermoelectric power in organic materials has emerged as a new area of research, mainly because of attractive characteristics, such as low thermal conductivity, mechanical flexibility, potential low cost, and large-area fabrication. In organic semiconductors and conductive polymers, the thermoelectric effect arises from the diffusion of charge carriers driven by a temperature gradient, analogous to that observed in inorganic materials. However, the charge transport mechanism is often localized, and unlike inorganic materials, the inherent disorder in molecular structure and arrangement leads to different behaviors, typically resulting in a higher Seebeck coefficient even though the electrical conductivity is usually less than that of inorganic substances. Optimization of the Seebeck coefficient, electrical conductivity, and thermal conductivity can be achieved by manipulating the molecular structure, doping levels, and processing methods towards a high thermoelectric figure of merit (zT).

This study attempts to investigate the role of limited conjugation, spiro connectivity, and molecular conformations in optoelectronic and thermoelectric thin films in the solid state. The addition of the spirothiadiazole moiety forms a three-dimensional, non-planar structure capable of inhibiting excessive intermolecular aggregation and, possibly, reduces lattice thermal conductivity, which is a desirable feature for thermoelectric materials. Three new spirothiadiazole–thieno[2,3-*b*]thiophene-based macro-heterocyclic compounds (**Kz1–Kz3**) were synthesized *via* an environmentally friendly process and used as model systems, and their optical, electrical, and thermoelectric characteristics were investigated. The potential of these compounds to be applied for thermoelectric generation was verified, and the related parameters were optimized.

2. Experimental

2.1. Preparation of thin films

The resultant thin films were placed onto clean glass substrates *via* spin coating with 0.003 g of the synthesized chemical diluted in 10 ml of alcoholic solution. The thickness of the thin films (300 ± 15 nm) was measured using a surface profilometer (FORM TALYSURF 50).

2.2. Materials and techniques

Using percolated dishes of silica gel G/UV-254 with a thickness of 0.25 mm (Merck 60F254) and UV light (254 nm/365 nm) to allow visualization, thin-layer chromatography (TLC) was used to monitor all reactions. All melting points were recorded using an uncorrected Kofler melting point instrument. The IR spectra were analyzed using an FT-IR spectrophotometer with KBr pellets. ^{13}C NMR (DMSO-d_6) and ^{1}H NMR spectra were recorded at Sohag University at 400 MHz and 100 MHz, respectively. Information on chemical shift, integration, and multiplicity (singlet, doublet, triplet, and multiplet) is given for ^{1}H NMR data. For internal measurement, tetramethylsilane (TMS) was chosen as the standard, and its chemical shifts (δ) were reported in parts per million (ppm). Internal standards for ^{13}C NMR were either DMSO (= 39.51 ppm) or TMS (= 0 ppm). The elemental analyses were performed using a PerkinElmer CHN analyzer model.

The absorbance, transmission, and reflection spectra were measured at normal incidence in the 200–2500 nm wavelength range using a computer-programmed double-beam spectrophotometer model Jasco 570 with a reflectivity attachment model ISN 470 (Japan). VTC-50A spin coating was employed to deposit thin coatings. Iodine doping was conducted at room temperature in a closed glass chamber, where the thin films were sealed under saturated iodine vapor at a constant distance of approximately 5 cm over 5 min. The D.C. electrical resistance of the present films was determined using a two-probe approach. These measurements were taken using a multimeter (model number HP HEWLTTPACKARD 34401). A silver paste electrode with a part spacing of 3 mm for the film was used. To regulate the sample temperature throughout the 430–520 K range, the films were put in a software tube centre. The annealing process was performed using a LINDBERG digital furnace.

Seebeck coefficient measurements were carried out in a conventional manner at a constant temperature difference ($\Delta T \sim 4$ degree) between the two ends of the film. The

temperature difference was determined by measuring separately the thermovoltages at the film ends using a Keithley 191 digital multimeter. The generated thermopower was measured using a Keithley 614 digital electrometer.

2.3. Synthesis of thienothiophene thiohydrazide Kz

In a round-bottomed flask, hydrazinecarbothiohydrazide **i** (0.002 mol) in 3 ml acetic acid as a catalyst and 15 ml ethanol was added to 1,1′-(3,4-dimethyl-3*a*,6*a*-dihydrothieno[2,3-*b*]thiophene-2,5-diyl)bis(ethan-1-one) **ii** (0.001 mol), and the reaction mixture was stirred under reflux for about five hours to afford (1*Z*,1′*Z*)-((3,4-dimethyl thieno[2,3-*b*]thiophene-2,5-diyl)bis(ethan-1-yl-1-ylidene))bis(hydrazine).

2.4. Synthesis of spirothiadiazole–thienothiophene-based macroheterocyclic compounds

Thienothiophene thiohydrazide **Kz** (0.001 mol) in 15 mL of ethanol was mixed with ketones **1a**, **b** (0.002 mol) or (0.001 mol) **1b**, and the reaction mixture was stirred under reflux for about three hours without any catalyst. The solid precipitate was filtered, washed with ethanol, and then left to dry.

2.4.1. 5′,5‴-(((1*Z*,1′*Z*)-(3,4-Dimethylthieno[2,3-*b*]thiophene-2,5-diyl)bis(ethan-1-yl-1-yl idene))bis(hydrazin-1-yl-2-ylidene))bis-(2*H*,3′*H*-spiro[acenaphthylene-1,2′-[1,3,4]thiadiazol]-2-one) (Kz1). Orange solid, yield = 96%. M.p. 218–220 °C. FT-IR (KBr) ν_{max} cm^{-1}: 3415, 3237(2NH), 3003($CH_{arom.}$), 2856($CH_{aliph.}$), 1685 (C═O_{amide}, st), and 1615 ((–HC═N–, st). ^{1}H-NMR (DMSOd_6), δ ppm: 14.19 (s, 1H, $NH_{hydrazone}$), 11.49 (s, 1H, $NH_{thiadiazole}$) 8.44–7.82 (m, 7H, $CH_{arom.}$); 3.44 (s, 3H, $CH_{3hydrazone}$) 2.65 (s, 3H, $CH_{3thiophene}$); ^{13}C-NMR (DMSO-*d*6), δ ppm: 182.45(C═O), 168.01(C═N), 159.00(C═N), 140.80, 140.54, 140.12, 135.03, 133.55, 132.62, 129.39, 129.57, 128.26, 127.23, 127.67, 126.05, 120.47($13C_{arom.}$), 82.43(C_{spiro}), 20.64($CH_{3hydrazone}$) and 10.45($CH_{3thiophene}$). C.F.: $C_{38}H_{28}N_8O_2S_4$, M.W.: 756.94. Elemental analysis: calc. C, C, 60.30; H, 3.73; N, 14.80; O, 4.23; S, 16.94; found, C, 60.63; H, 3.92; N, 14.57; S, 16.60.

2.4.2. 5′,5‴-(((1*Z*,1′*Z*)-(3,4-Dimethylthieno[2,3-*b*]thiophene-2,5-diyl)bis(ethan-1-yl-1-yli dene))bis(hydrazin-1-yl-2-ylidene))bis-(3′*H*-spiro[indoline-3,2′-[1,3,4]thiadiazol]-2-one) (Kz2). Orange solid, yield = 98%. M.p. 205–207 °C. FT-IR (KBr) ν_{max} cm^{-1}: 3413, 3316, 3232(3NH), 3003($CH_{arom.}$), 2814($CH_{aliph.}$), 1733(C═O_{isatin}, st), 1697 (C═O_{amide}, st), and 1619 ((–HC═N–, st). ^{1}H-NMR (DMSOd_6), δ ppm: 14.23 (s, 1H, $NH_{hydrazone}$), 11.51 (s, 1H, $NH_{thiadiazole}$) 7.60–7.40 (m, 5H, $CH_{arom.}$); 3.44 (s, 3H, $CH_{3hydrazone}$) 2.68 (s, 3H, $CH_{3thiophene}$); ^{13}C-NMR (DMSO-*d*6), δ ppm: 175.63(C═O), 163.71(C═N), 158.47(C═N), 141.58, 139.36, 137.43, 131.53, 129.30, 162.97, 123.34, 120.35, 110.78($9C_{arom.}$), 80.67(C_{spiro}), 20.49 ($CH_{3hydrazone}$) and 10.94 ($CH_{3thiophene}$). C.F.: $C_{30}H_{26}N_{10}O_2S_4$, M.W.: 686.85. Elemental analysis: calc. C, C, 52.46; H, 3.82; N, 20.39; O, 4.66; S, 18.67; found, C, 52.23; H,3.70; N, 20.68; O, 4.33, S, 18.91.

2.4.3. 2,2′-[(Disulfanediylbis(1*H*-benzo[*d*]imidazole-2,1-diyl))-bis(naphthalene-1,1′-diyl)]bis(dithieno [3,2-*b*:2′,3′-*d*]pyrrole) (Kz3). Orange solid, yield = 91%. M.p. 198–200 °C. FT-IR (KBr) ν_{max} cm^{-1}: 3414, 3236(2NH), 3003($CH_{arom.}$), 2925($CH_{aliph.}$), and 1615 ((–HC═N–, st). ^{1}H-NMR (DMSOd_6), δ ppm: 14.21 (s, 1H, $NH_{hydrazone}$), 11.51 (s, 1H, $NH_{thiadiazole}$) 8.33–7.82 (m, 6H, $CH_{arom.}$); 3.40 (s, 3H, $CH_{3hydrazone}$) 2.72 (s, 3H, $CH_{3thiophene}$); ^{13}C-NMR (DMSO-d_6), δ ppm: 158.47(C═N), 151.64(C═N), 141.68, 139.36, 137.43, 131.53, 129.30, 126.97, 126.39, 123.34, 120.35, 110.78($13C_{arom.}$), 80.67(C spiro), 21.74($CH_{3hydrazone}$) and 10.77. ($CH_{3thiophene}$); C.F.: $C_{26}H_{22}N_8S_4$, M.W.: 574.09. Elemental analysis: calc. C, C, 54.33; H, 3.86; N, 19.50; S, 22.31; found, C, 54.00; H,4.01; N, 19.20; S, 21.95.

3. Results and discussion

3.1. Chemistry

In continuation of our work in the synthesis of novel spiroheterocycles,[22–26] we prepared a new series of spirothiadiazole–thienothiophene-based macroheterocyclic derivatives containing a 1,3,4-thiadiazole moiety. Stirring thienothiophene thiohydrazide **1** under reflux with ketones **1a–c** in ethanol under green conditions afforded spirothiadiazole–thienothiophene-based macro heterocyclic derivatives **Kz1–Kz3** (Scheme 1).

3.2. Film microstructures

As shown in X-ray diffractograms (Fig. 1), **Kz1**, **Kz2**, and **Kz3** are entirely amorphous microstructures.[27]

3.3. Investigation of optical properties

3.3.1. Optical analysis. Fig. 2 illustrates the transmission and absorption spectra in the wavelength (λ) range of 300–2500 nm for the present compound's thin films. Fig. 2a reveals that the fundamental absorption edge for the compounds **Kz1**, **Kz2**, and **Kz3** exists in the wavelength range of $330 < \lambda < 380$ nm (barely in the UV-vis regions), which may be related to π–π* transition.[28,29] The compound **Kz1** shows high transmission of nearly 65–70% at a wavelength in the range of 500 to 2500 nm. However, compounds **Kz2** and **Kz3** start with high transmission (~70%) and then gradually decrease with the increasing energy from NIR to ~UV spectral regions. This decrease in transmission can be attributed to the increase in absorption with the increase in $h\nu$, as shown in Fig. 2b.

Measured transmission and reflection spectra were utilized to compute optical parameters including absorption coefficient α, refractive index n, and extinction coefficient k. When numerous reflections are neglected in a perfectly flat film and the substrate, the optical transmission T and subsequent α, n, and K can be obtained using the following equations:[30,31]

$$T = (1 - R)^2 \exp(-A) \quad (1)$$

$$\alpha = \frac{\mathrm{Abs}}{d} = \frac{2.303}{d} \log\left[\frac{(1-R)^2}{T}\right] \quad (2)$$

$$n = \left(\frac{1+R}{1-R}\right) + \left[\left(\frac{1+R}{1-R}\right)^2 - \left(1 + K^2\right)\right]^{\frac{1}{2}} \quad (3)$$

and

$$K = \alpha\lambda/4\pi, \quad (4)$$

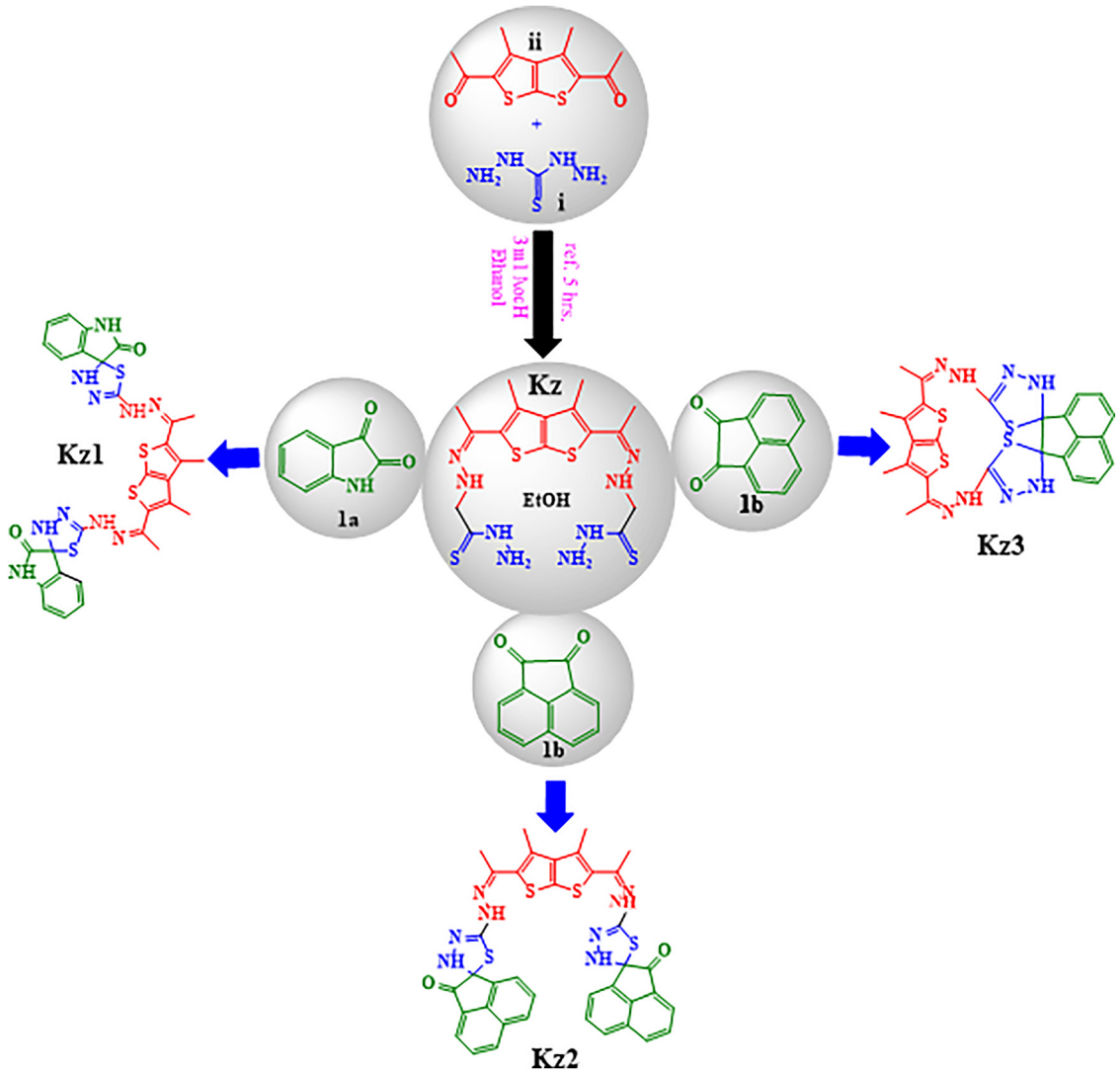

Scheme 1 Synthesis of spirothiadiazole–thienothiophene-based macroheterocyclic derivatives **Kz1–Kz3**.

where d is the film thickness.

The spectral variations of refractive index (n) and extinction coefficient are important in various areas. The refractive index controls light refraction and transmission, while the coefficient of extinction determines light absorption. These optical constants are essential for design and adaptation in understanding optical devices, photonic components and even physical properties at a fundamental level.[32,33] Table 1 shows the average values of the absorption coefficient (α_{500}) and refractive index (n_{500}) in the solar maximum wavelength (λ = 500 nm) in comparison with the corresponding reported values of some organic materials.

The compound thin films (**Kz1**, **Kz2**, and **Kz3**) exhibit a high refractive index (n) around the UV region (Fig. 3a). A prominent peak appears at 473 to 605 nm, which may be due to considerable absorption generated by electronic transitions around the band gap energy. The elevated refractive index over that area suggests that the material is significantly polarized. In addition, the refractive index in general shows normal dispersion behavior. Fig. 3b depicts the extinction coefficient of thin films of compounds **Kz1**, **Kz2**, and **Kz3**, revealing that the extinction coefficient is high in the UV region, drops sharply near the fundamental absorption edge, and finally, increases once again in the wavelength range of 500 to 2500 nm. Such behavior looks like and reflects the corresponding absorption spectrum (Fig. 2b).

In the range of $1 < \alpha\ (\mathrm{cm}^{-1}) < 10^4$, α varies exponentially with photon energy ($h\nu$), based on the density and tail width (E_u) of the localized states, which generally occur in the band gap region of the amorphous non-metallic semiconductors, verifying the following Urbach relation:[34]

$$\alpha = \alpha_0 \exp\left(\frac{h\nu}{E_u}\right) \quad (5)$$

In this equation, α_0 is a constant and E_u is the energy width of localized states. The E_u values were computed using the slopes of the $\ln\alpha$ *vs.* $h\nu$ plots (Fig. 4) and documented in

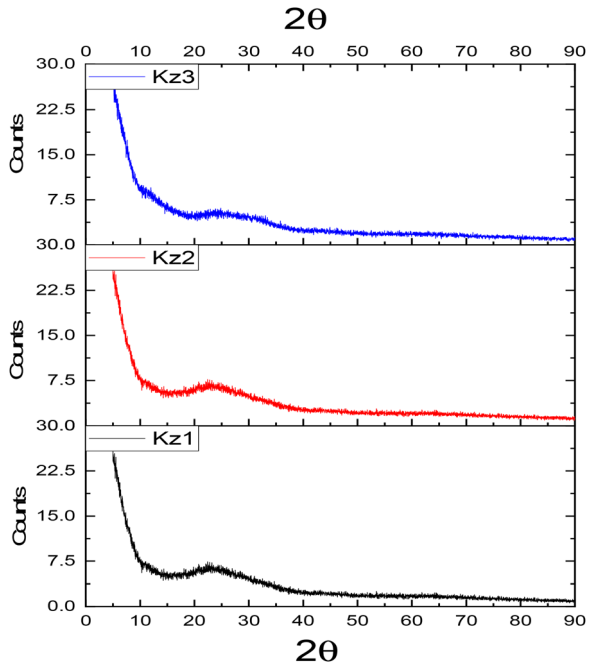

Fig. 1 XRD patterns of the thin films (300 ± 15 nm) of **Kz1**, **Kz2** and **Kz3**.

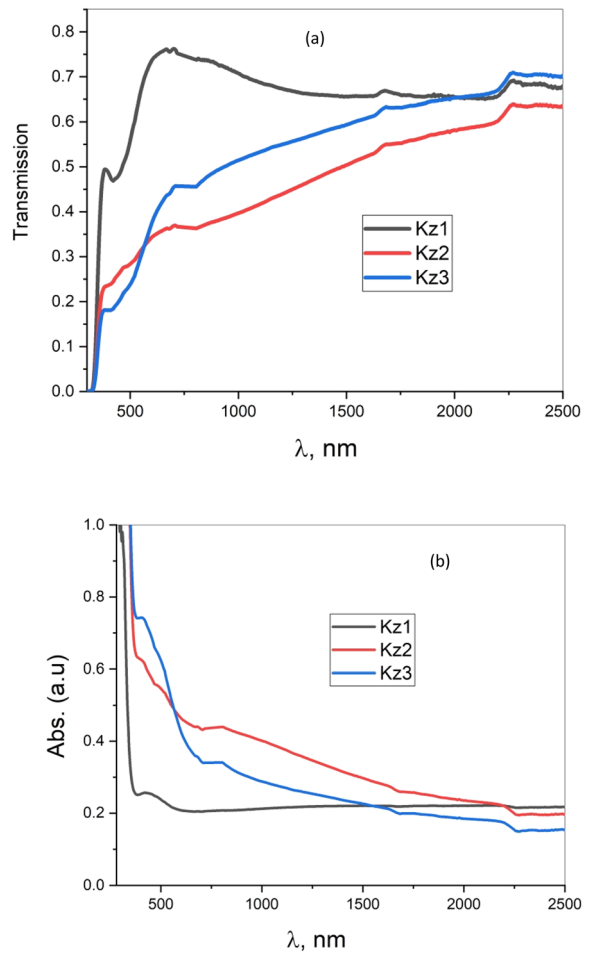

Fig. 2 Transmission (a) and absorption (b) spectra of the thin films of **Kz1**, **Kz2** and **Kz3**.

Table 1. The E_u values of thin films of compounds **Kz3** > **Kz2** > **Kz1** can correspond to the microstructure and/or π-conjugation number.[4,35,36]

The penetration depth δ is a vital optical characteristic that indicates how far incident light could penetrate a substance before its intensity is noticeably reduced. It is also related to the absorption coefficient, and heavily relies on the wavelength and physical structure of the substance. The penetration depth could be determined using the following equation:

$$\delta = \frac{\lambda}{4\pi k} = \frac{1}{\alpha}\ \text{cm}$$

Fig. 5 demonstrates that the compound **Kz3** has a high penetration depth in the wavelength region of 1500 to 2500 nm, which can be attributed to its low extinction coefficient, making it a potential material for IR sensors. Compound **Kz1** exhibits a high extinction coefficient; therefore, its penetration depth is high in the 300–1500 nm wavelength range, making it appropriate for surface-sensitive device uses.

The Moss criterion[37] can be used to estimate absorption transitions and band gap energies. The band gap value E_g is calculated by determining the value of λ that occurs when the slope of the absorption coefficient is maximum near the absorption edge.[38–41] The absorption coefficient of a thin layer might be expressed as follows:[12,31,42]

$$(\alpha h\nu) = \beta(h\nu - E_g)^r \quad (6)$$

and

$$\ln(\alpha h\nu) = r\ln(h\nu - E_g) + \ln\beta \quad (7)$$

The transition exponent (r) in eqn (6) was determined from eqn (7), as described elsewhere.[43] The value of (r) was found to be equal to ~2 for all the present compounds, indicating indirect allowed transition. Using $(\alpha h\nu)^{\frac{1}{2}}$ *vs.* $h\nu$ plots (Fig. 6), the values for the energy of the band gap (E_g) of thin films of compounds **Kz1**, **Kz2** and **Kz3** were determined from extrapolations to $h\nu = 0$. The UV vis absorption spectra of the **Kz1–Kz3** thin films show absorption onsets, which are placed in the near UV range and give optical band gaps covering the 2.99 to 3.26 eV. These relatively broad band intervals are supported by the decimated π-conjugated and the non-planar molecular structures imposed by the spiro conjunction and by the thieno[2,3-*b*]thiophene core.

As noted in Table 1, these values were found to be equivalent to those published for numerous conjugated organic materials.

The optical conductivity is a key measurement that tells how well a material works to carry electric charges when an electromagnetic field is moving. It gives us an improved understanding of how photons that strike the material interact with free carriers or localized states. We used the measured refractive index (n) and absorption coefficient (α) to find the optical conductivity (σ_{opt}) using the following equation:[45]

$$\sigma_{opt} = \frac{\alpha n c}{4\pi}$$

where c is the speed of light and λ is the wavelength.

Table 1 Values of energy band gap E_g, Urbach energy E_u, absorption coefficient α_{500}, and refractive index n_{500} for the **Kz1**, **Kz2**, and **Kz3** thin films compared with those for the previously reported conjugated organic materials

	α_{500} (cm^{-1}) × 10^5	n_{500}	E_g (eV)	E_u (eV)	Ref.
Compound **Kz1**	0.95	1.47	3.26	3.12	Present
Compound **Kz2**	2.18	1.85	3.17	2.27	work
Compound **Kz3**	2.5	1.97	2.99	0.96	
TT amino cyano + 1-naphthyl amine	3.4	1.55	2.79	1.04	13
3,4-Diamino-*N*′2,*N*′5-bis(2-oxoindolin-3-ylidene)thieno[2,3-*b*]thiophene-2,5-dicarbohydrazide	5.6	1.92	2.7	1.45	10
3′-Acetyl-5′-amino-2′-methyl-2-oxo-7′-(thiophen-2-yl)spiro[indoline-3,4′-pyrano[2,3-*b*]pyridine]-6′-carbonitrile	0.7	2.06	3.56	—	12
p-tert-Butylthiacalix[4]arene derivatives		4.2	2.9	1.23	44

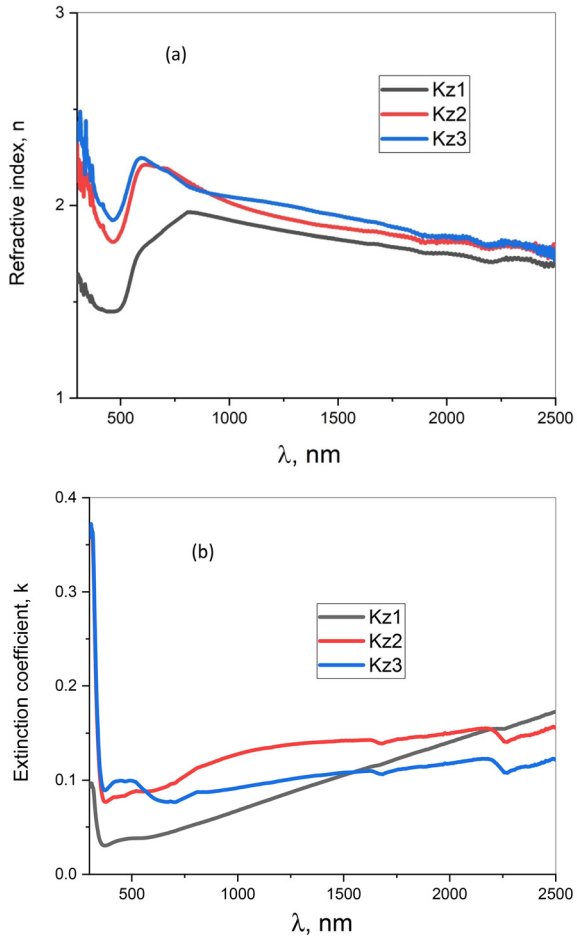

Fig. 3 Refractive index n (a) and extinction coefficient k (b) spectra of the thin films of **Kz1**, **Kz2** and **Kz3**.

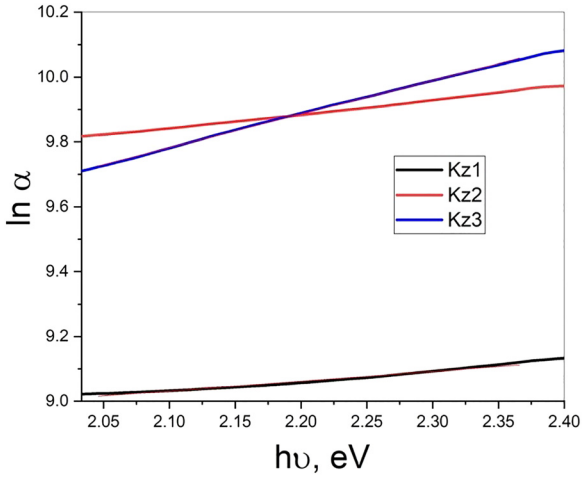

Fig. 4 : Plots of ln α *vs.* $h\nu$ of the thin films of **Kz1**, **Kz2** and **Kz3**.

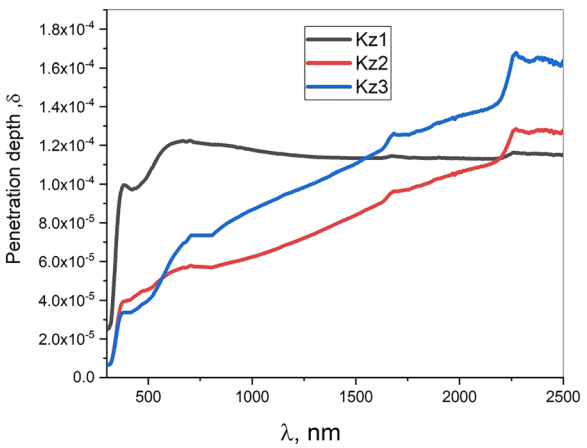

Fig. 5 Light wavelength dependence of the penetration depth of the thin films of **Kz1**, **Kz2** and **Kz3**.

Fig. 7 exhibits that strong interband electronic transitions close to the fundamental absorption edge cause all samples to have the highest optical conductivity in the ultraviolet wavelength range (about 400 nm). The optical conductivity gradually decreased as the wavelength increased through the visible and near-IR range, which is consistent with lower photon energy and decreasing absorption. Furthermore, compared to **Kz1** and **Kz3**, **Kz2** exhibits larger optical conductivity in the area of longer wavelength region. This suggests that there are more free carriers or defect states present, which improve sub-bandgap absorption. However, **Kz1**'s lower Urbach energy and higher refractive index are consistent with its lower optical conductivity at higher wavelengths, suggesting enhanced crystallinity and less structural disorder. The obtained results show that modifying the film's composition and quality of structure

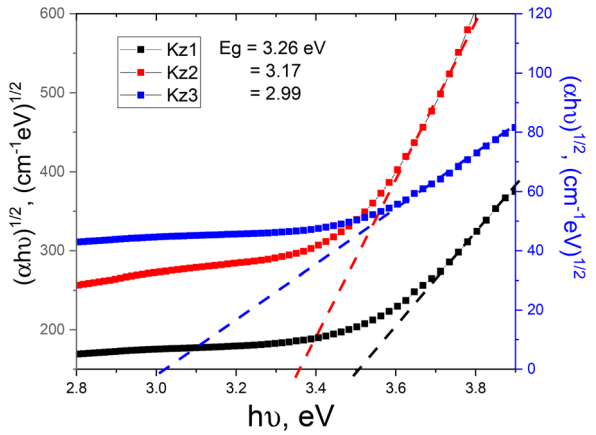

Fig. 6 $(\alpha h\nu)^{\frac{1}{r}}$ *vs.* $h\nu$ plots of the thin films of **Kz1**, **Kz2** and **Kz3**.

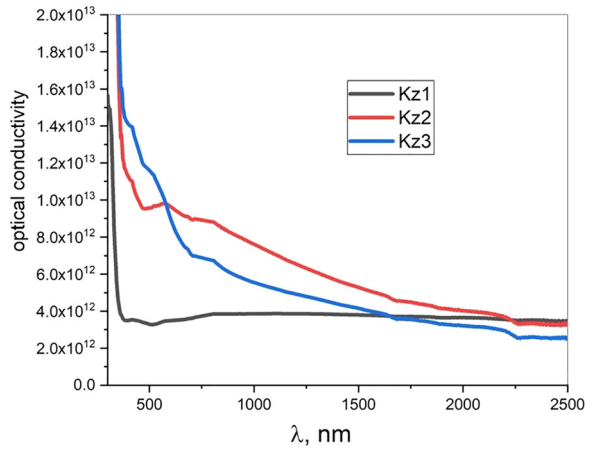

Fig. 7 Variation in the optical conductivity of the thin films of **Kz1**, **Kz2** and **Kz3**.

may enhance its optical conductivity for optoelectronic applications including photodetectors and transistors, as well as absorber layers, where controlling the way light interacts with the material and the way carriers move is significant for device performance.

3.3.2. Dielectric and dispersion characterization. The dielectric constant (ε) is a crucial metric for understanding electronic transitions and excitonic properties in semiconductors.[46,47] Materials with greater values of ε are endowed with inherent charge carriers.[48] In normal dispersion, ε' decreases with λ^2, indicating increased free carrier absorption and suggesting a gradual decline in optical absorption with the increase in wavelength. The following equations can be used to calculate dielectric parameters in thin films, including the lattice dielectric constant ε_L, the ratio of carrier concentration N to m (N/m, where m is the ratio of carrier effective mass to the electron rest mass (m^*/m_0)), the contribution of free carrier susceptibility χ_c to the real dielectric constant, and the plasma frequency (ω_p):[49]

$$\varepsilon' = n^2 - k^2 = \varepsilon_L - \frac{e^2}{\pi c^2 m_0} \times \left(\frac{N}{m}\right)\lambda^2$$

$$= \varepsilon_L + 4\pi\chi_c \quad (8)$$

$$\omega_p = \frac{2\pi C}{\lambda_p} = \left(\frac{Ne^2}{\varepsilon_0 m_0}\right)^{1/2} \quad (9)$$

and

$$N = \frac{\varepsilon_0 m_0}{e^2}\omega_p{}^2 \quad (10)$$

where λ_p is the plasma wavelength (the λ value at $\varepsilon' = 0$), e is the electronic charge, and c is the speed of light. The results showed that compound **Kz2** had high dielectric characteristics, which might be attributable to its large absorption. Table 2 contains the computed dielectric parameters based on the $\varepsilon' - \lambda^2$ graphs shown in Fig. 8a.

Di Domenico and Wemple[50] proposed a single oscillator model to explain the relationship between the refractive index and the photon energy in the normal dispersion region. The equation is as follows:

$$(n^2 - 1)^{-1} = \frac{E_o}{E_d} - \frac{1}{E_o E_d}(h\nu)^2 \quad (11)$$

E_o and E_d are the oscillator and dispersion energies, respectively.

Fig. 8b depicts the $(n^2 - 1)^{-1}$ *vs.* $(h\nu)^2$ plots of thin films of compounds **Kz1**, **Kz2** and **Kz3**. The oscillator energy (E_o) and dispersion energy (E_d) can be derived from the slope $(E_o E_d)^{-1}$ of the linear component of the plot and the intercept (E_o/E_d) with

Table 2 Comparison of the dielectric and dispersion properties of the current samples with those reported previously

	E_o (eV)	E_d (eV)	ε_L	N/m^* (10^{17} cm^{-3} g^{-1})	$\lvert\chi_c\rvert$	ω_p, s^{-1} × 10^{14}	Ref.
Compound **Kz1**	1.74	3.17	3.86	2.74	0.74	12.0	Present
Compound **Kz2**	1.75	3.57	4.14	3.06	0.75	12.5	work
Compound **Kz3**	1.77	3.94	4.49	3.47	0.77	12.8	
PPY film	2.37	—	2.94	0.95	0.32	5.52	38
TT amino ester	2.15	2.95	3.29	0.034	0.16	3.31	51
Diethyl3,4-bis(((*E*)-2-xoindolin-3-ylidene)amino)thieno[2,3-*b*]-thiophene	2.16	3.86	4.47	0.057	0.27	1.35	5
3,4-Diamino-*N*′2,*N*′5-bis(2-oxoindolin-3-ylidene)thieno[2,3-*b*]-thiophene-2,5-dicarbohydrazide	4.5	2.7	4.51	0.86	0.034	5.25	10
TT amino cyano + 1-naphthyl amine	2.29	5.45	5.61	—	0.44	—	13

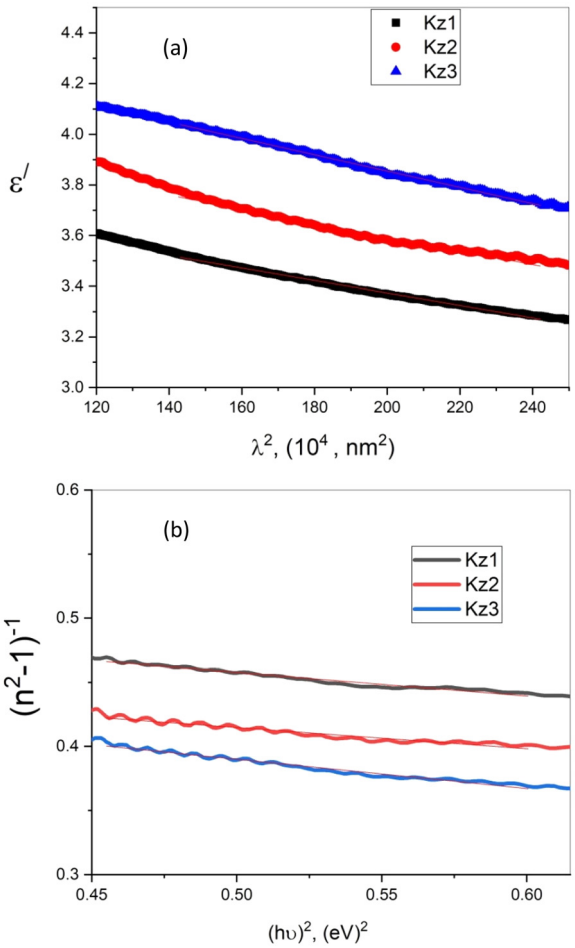

Fig. 8 $\varepsilon' - \lambda^2$ (a) and $\varepsilon'' - \lambda^2$ (b) plots of the thin films of **Kz1**, **Kz2** and **Kz3**.

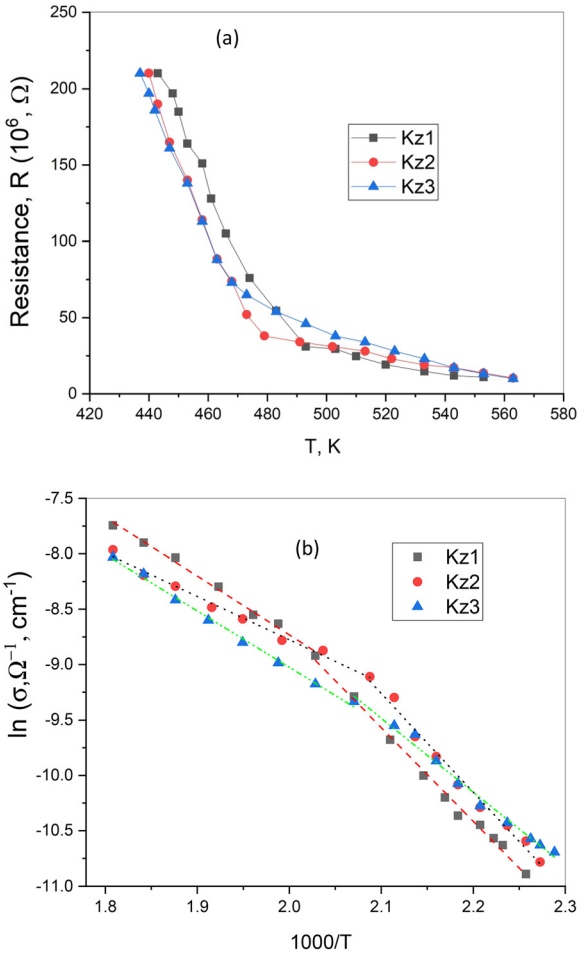

Fig. 9 Plots of DC-electrical resistance R *vs.* T (a) and ln(σ_{DC}) *vs.* (1000/T) (b) of the thin films of **Kz1**, **Kz2**, and **Kz3**.

the ordinate axis, where $E_o = \left(\frac{\text{intercept}}{\text{slope}}\right)^{1/2}$ and E_d = (slope × intercept)$^{-1/2}$.

The dielectric and dispersion properties were documented and compared with those of several conjugated organic compounds, as presented in Table 2.

3.3.3. Thermoelectric characterization and performance. The typical interrelation of the Seebeck coefficient and electrical conductivity, which are functions of charge carrier concentration and mobility, makes it essential to identify the electrical transport mechanism in the present organic compounds. Fig. 9a depicts the DC-electrical resistance (R) of thin films of compounds **Kz1**, **Kz2**, and **Kz3** at temperatures ranging from 437 to 553 K. The original **Kz1**, **Kz2**, and **Kz3** thin films have a comparatively high overloaded resistance at RT due to their gluttonous tendency to oxygen absorption. Furthermore, the adsorbed atmospheric oxygen molecules can grab n-type conduction electrons, reducing electron concentration and resulting in an overloaded amount of film resistance. The measurable R-values of 21 × 10^7 Ω were achieved at ∼437 K and decreased to 11 × 10^6, 10.3 × 10^6, and 10 × 10^6 Ω for thin-film **Kz1**, **Kz2**, and **Kz3** compounds, respectively, at ∼553 K, indicating semiconducting behavior.

This may demonstrate that the adsorbed oxygen can be thermally liberated over the film surface, leading to an increase in sample conductivity.

The following Arrhenius relationship[52–54] may calculate the conduction activation energy in the visible resistance ranges, where

$$\sigma_{DC} = \sigma_1 \exp\left(\frac{-\Delta E_{\sigma_1}}{k_B T}\right) + \sigma_2 \exp\left(\frac{-\Delta E_{\sigma_2}}{k_B T}\right) \quad (12)$$

ΔE_{σ_1} and ΔE_{σ_2} and σ_1 and σ_2 represent the thermal activation energies associated with the conduction and the pre-exponential factors corresponding to lower and higher temperature ranges, respectively. k_B is Boltzmann's constant. Fig. 9b reveals that the graphs of ln σ *vs.* 1000/T are straight. The activation energy for electrical conduction represents energy barriers, which charge carriers must overcome in order to flow. Thin-film **Kz1**, **Kz2**, and **Kz3** compounds have ΔE_{σ_1}, ΔE_{σ_2} values of (0.76, 0.40), (0.72, 0.36) and (0.57, 0.16), in the lower and higher temperature ranges, respectively. Compound **Kz1** has the highest activation energy value, suggesting that charge carriers need higher amounts of energy to become mobile. However, the thin-film compound

Kz3 has the lowest activation energy, which could be ascribed to the continuous conjugation effect, which increases the hopping conduction. The values of ΔE_σ are similar to computed values for various organic semiconductor materials.[55,56]

The Seebeck coefficient is an extremely important thermoelectric material property. It is the voltage generated by a material when a temperature differential exists. The Seebeck coefficient ($\mu V\ K^{-1}$–$mV\ K^{-1}$) indicates the charge carrier (either holes or electrons) flow from the hot side to the cold side of the sample that causes the potential (voltage) decrease. The Seebeck coefficient also dictates the charge carrier type (positive charge carriers-holes; negative charge carriers-electrons) as well as if the material is having degenerate or non-degenerate transport properties.

3.3.4. Structure–property relationship. The distinctions of the thermoelectric behaviors in **Kz1**, **Kz2** and **Kz3** can be explained by the molecular structures and conformations of the synthesized compounds. **Kz2** takes a linearly expanded coil geometry, as shown in Scheme 1, whilst **Kz1** and **Kz3** have smaller geometries. This extended structure in **Kz2** allows interchain π–π* stacking and is good at charge carrier mobility, as indicated by the higher electrical conductivity and the power factor of **Kz2** relative to the other two substances. This stiffness of the spirothiadiazole–thieno[2,3-*b*]thiophene unit of **Kz1** contributes to a higher threshold to electrical conduction (ΔE_{σ_1} = 0.76 eV), and therefore, the conductivity is lower. Conversely, **Kz3**, even with a benzimidazole group atom, has seen an intermediate performance because of the presentation of a disulfide bond that partially breaks the conjugated performance. Such observations put a stress on the concept that thermoelectric performance cannot just be determined by the total length of the π-conjugation, but is also largely determined by the molecular structure and the level of order within the thin film.

The electrical and thermal properties of a thermoelectric material can be correlated through the figure of merit z, K^{-1} or the dimensionless zT, where:

$$z = \frac{s^2}{\rho \hbar} \tag{13}$$

and

$$zT = \frac{s^2 T}{\rho \hbar} = \frac{\left(S_n - S_p\right)^2 T}{\left[\left(\rho_n \hbar_n\right)^{\frac{1}{2}} + \left(\rho_p \hbar_p\right)^{\frac{1}{2}}\right]^2}, \tag{14}$$

where S, ρ and $\hbar$ are the Seebeck coefficient, electrical resistivity and thermal conductivity, respectively. $T = [T_h + T_c]/2$ is the average temperature between the temperatures of the hot and cold sides (T_h and T_c, respectively). n and p refer to n- and p-type semiconductors. zT typically indicates the thermoelectric performance.

The ideal thermoelectric materials are characterized by low values of both $\hbar$ and ρ to increase the temperature gradient and decrease Joule heat, respectively. This leads to maximizing the participation of the obtainable charge carriers in the thermoelectric effect. Besides, the Seebeck coefficient S depends on the Fermi-level energy position and material structure that is affected mainly by the charge carrier density and temperature. Moreover, the thermal conductivity $\hbar$ of a material results from lattice vibrations (phonons) $\hbar_l$ and charge carrier (electron) $\hbar_e$ components:

$$i.e.\ \hbar = \hbar_l + \hbar_e \tag{15}$$

3.3.4.1. Thermal conductivity estimation method. The Wiedemann–Franz law[57,58] was used to estimate the total thermal conductivity $\hbar_e$ in this research, and the electronic thermal conductivity $\hbar_e$ is generally proportional to the electrical conductivity σ. For organic materials, this law is often represented as follows:

$$\hbar_e = LT\sigma, \tag{16}$$

where $L = 2.44 \times 10^{-8}\ W\Omega\ K^{-2}$ is the Lorenz number.

In accordance with the decrease in both S and ρ, while $\hbar_l$ increases with the increasing charge carrier concentration, the metals reveal small values of zT unlike insulators that possess relatively high values of zT due to their small $\hbar$ and high ρ and S values. This encourages us to expect that the optimal carrier concentration values could be almost close to 10^{17}–$10^{19}\ cm^{-3}$ characterizing the range of the critical case between the degenerate and non-degenerate semiconductors. Due to the fact that $\hbar_e$ was not determined experimentally, the values of zT are not the real values but the approximated upper limits. However, since the similar estimation technique was implemented across all the samples, the comparative trends among **Kz1–Kz3** and under different treatment conditions remain valid. The heat conductivity of organic semiconductors is normally dominated by the lattice thermal conductivity; thus, the values of the zT are reported as upper-bound values but not as absolute values.

3.3.5. Optimization of thermoelectric performance. The performance of thermoelectric can be optimized using various methods, which may include optimization of carrier concentration, carrier mobility, and electrical and thermal conductivities. In this work, the organic compounds, with their specific conformations, conjugation numbers and therefore various carrier concentrations, were studied over a series of temperatures.

As shown in Fig. 9 and 10, the simultaneous increase and decrease in σ and S, respectively, with the increase in temperature could be attributed to the mixed conduction (by both electrons and holes) and their behaviors to the same factors. These results can be described by the following two unlike carrier's mechanisms,[40] where

$$\sigma = en\mu_n + ep\mu_p = en\mu_n\left[1 + \left(\frac{p}{n}\right)\left(\mu_p/\mu_n\right)\right] \tag{17}$$

and

$$(-S) = \frac{|S_n|\mu_n n - |S_p|\mu_p p}{\mu_n n + \mu_p p} = \frac{|S_n| - |S_p|\left(\mu_p/\mu_n\right)\left(\frac{p}{n}\right)}{1 + \left(\mu_p/\mu_n\right)\left(\frac{p}{n}\right)}, \tag{18}$$

where S_n, μ_n & n and S_p, μ_p & p are the Seebeck coefficient, mobility and density of electrons and holes, respectively. Thus,

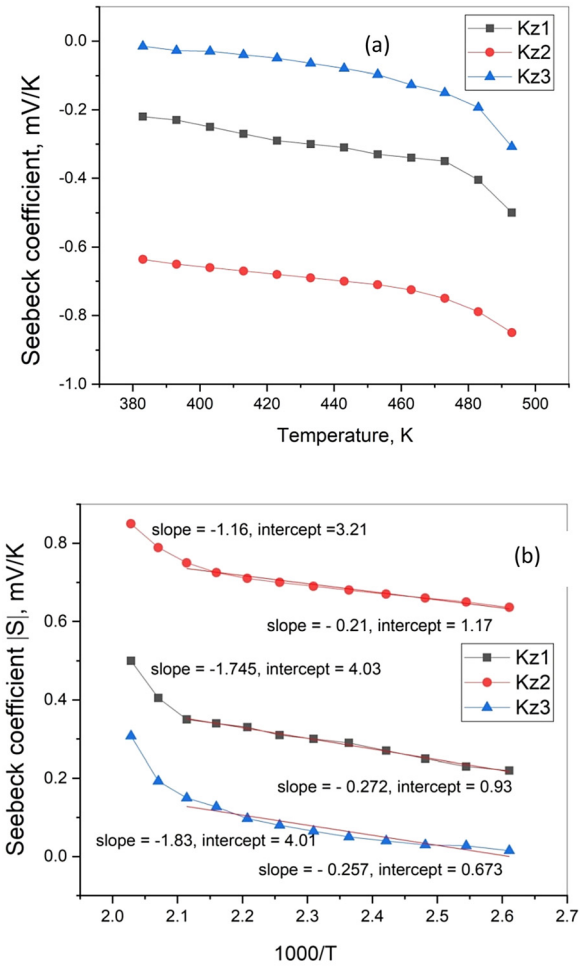

Fig. 10 Seebeck coefficient *vs* temperature plots (a) and *versus* 1000/T (K^{-1}) plots (b) for compound **kz1**, **kz2**, and **kz3** thin films.

the changes in σ and S with the increase in temperature are associated with the changes in p/n and/or μ_p/μ_p ratios caused by temperature.

The S–T plots given in Fig. 10a show that the Seebeck coefficient values of **Kz1**, **Kz2** and **Kz3** thin films are relatively high (mV K^{-1} units), which are comparable to the S values for some inorganic materials.[59–61] Besides, the negative sign of S is indicative of n-type thermoelectric materials. If large, the Seebeck coefficient also indicates that the Fermi level is very low below the conduction band edge, generally related to lower carrier densities or more energy-dependent scattering. The different values obtained for the Seebeck coefficient by the present compounds may mainly depend on the different conjugation numbers in the compounds' structures. As shown in Table 3, the **Kz2** compound thin film has the largest negative Seebeck coefficient values of −0.71 mV K^{-1} and −0.85 mV K^{-1}, indicating extensive thermoelectric voltage generation. The high thermoelectric performance observed for compound **Kz2**, compared to **Kz1** and **Kz3**, is consistent with expectations. Unlike the other two compounds, **Kz2** contains a larger conjugation number with a linearly expanded coil conformation

Table 3 Average values of the Seebeck coefficient of present compounds over the considered temperature ranges

Sample	T (K)	σ (Ω cm)$^{-1}$ × 10^{-5}	$-S$ (mV K^{-1})	$e^{Ef/kT}$	N, cm^{-3}	zT
Kz1	453	2.90	0.097	0.01	5.34×10^{17}	0.18
	463	3.70	0.127	0.04	2.11×10^{18}	0.19
	473	6.30	0.15	0.06	3.60×10^{18}	0.19
	483	9.20	0.193	0.08	4.84×10^{18}	0.21
	493	15.1	0.31	0.12	7.09×10^{18}	0.24
Kz2	453	3.40	0.71	1.92×10^{-5}	1.00×10^{17}	0.57
	463	5.38	0.72	2.56×10^{-5}	1.38×10^{17}	0.59
	473	9.15	0.75	6.11×10^{-5}	3.41×10^{17}	0.59
	483	12.1	0.83	8.66×10^{-5}	4.99×10^{17}	0.62
	493	17.2	0.85	9.73 × 10−5	5.78×10^{17}	0.67
Kz3	453	3.45	0.31	0.001	5.82×10^{16}	0.10
	463	4.21	0.33	0.002	1.20×10^{17}	0.12
	473	6.52	0.35	0.006	3.35×10^{17}	0.14
	483	8.81	0.44	0.007	4.60×10^{17}	0.18
	493	10.3	0.50	0.008	5.99×10^{17}	0.20

(Scheme 1). This extended conformation has been known to increase the mobility of charge carriers, and thus, enhance the thermoelectric performance of organic material.[62–65]

Besides, the temperature dependence shows that there is a moderate to very large increase in the Seebeck coefficient size

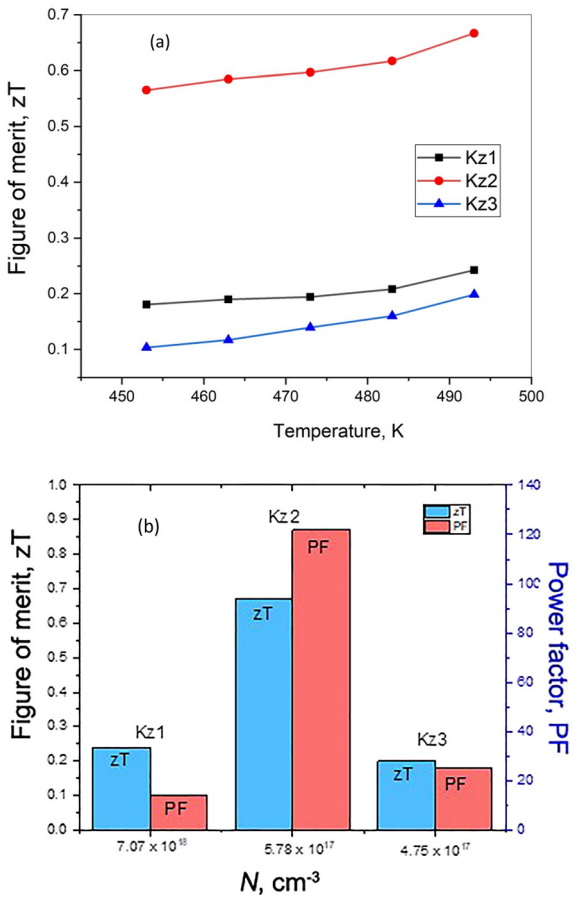

Fig. 11 zT *vs.* T plots (a), and zT and PF at optimal carrier concentrations (at T = 493 K, $\Delta T \sim 4$ °C) (b) of the thin films of **Kz1**, **Kz2**, and **Kz3**.

during temperature increase, specifically for **Kz1**, **Kz2**, and **Kz3**, which is indicative of a non-degenerate semiconductor's behavior.[66] This illustrates that the heating of the carriers is a significant factor in the transport process.

To confirm whether the charge carrier system in the organic compounds, which are physically regarded as often amorphous semiconductors, is degenerate or non-degenerate, the concept of the Fermi level could be utilized. It is represented by the chemical potential of electrons in the system at 0 K, and separated from the conduction band minimum value E_c (LUMO) by the energy value E_f that can be termed the carrier activation energy.[67,68]

The degeneracy of the electron gas is the case in which the number of carrier particles is comparable to the number of allowed states, *i.e.*, when the probability Fermi function $f(E)$ approaches unity:

$$f(E) = \frac{1}{e^{(E-E_f)/kT} + 1} \cong 1, \tag{19}$$

where $E = E_c = 0$ for the n-type semiconductor.

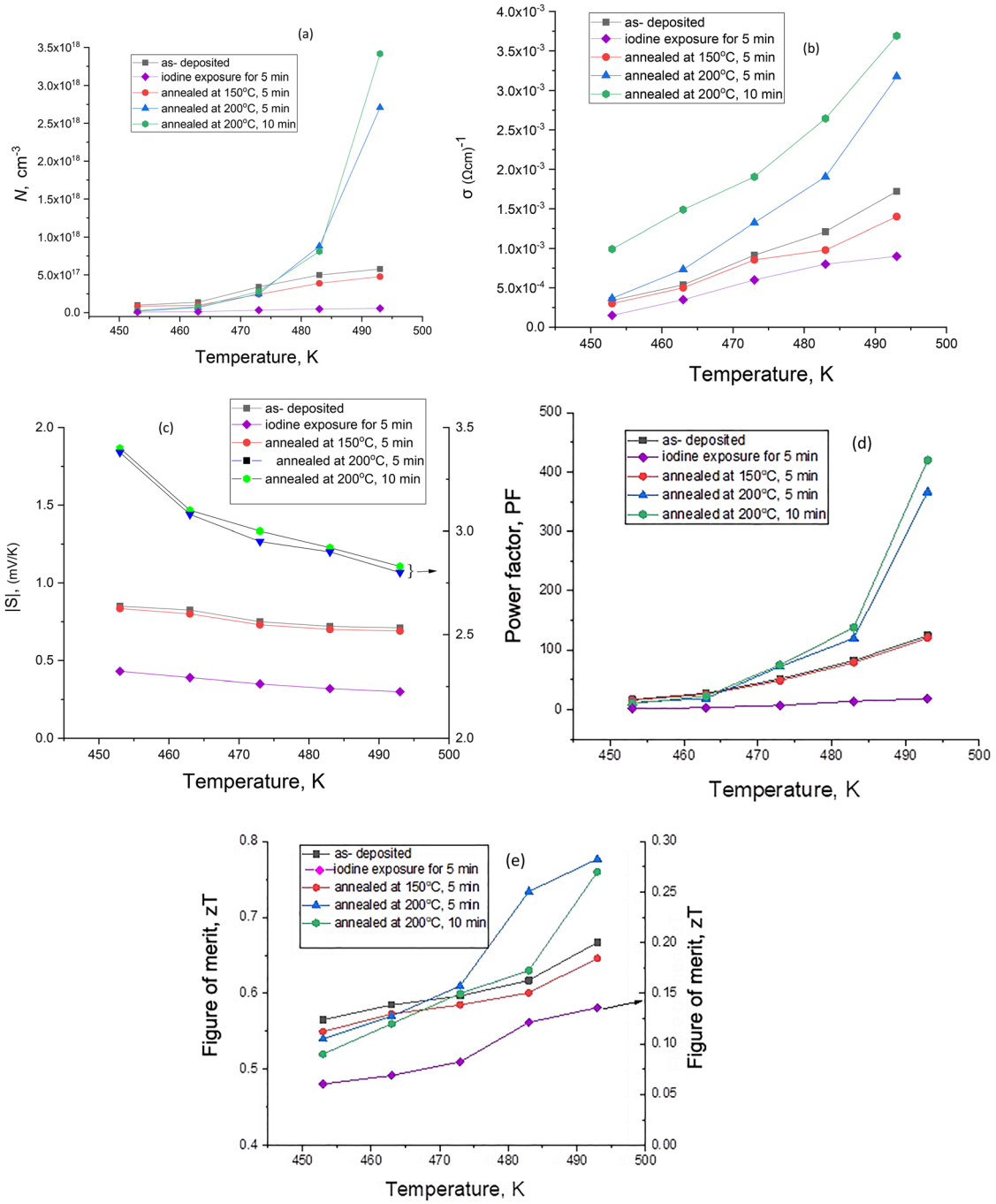

Fig. 12 Variations in N, cm^{-3} (a), σ, (Ω cm)$^{-1}$ (b), S, mV K^{-1} (c), PF (μW m^{-1} K^{-2}) (d) and zT (e) of the thin-film of **Kz2** under different conditions.

This means that $e^{E_f/kT} \gg 1$ and E_f has a positive value. The electron gas is non-degenerate when $f(E) \ll 1$ and $e^{E_f/kT} \ll 1$ or E_f has a negative value.

Besides, the Fermi-level energy (E_f) can be correlated with the Seebeck coefficient according to Benco and Koffyberg:[69]

$$S = \frac{k_B}{e}\left(\frac{E_f}{kT} + A\right) \quad (20)$$

or

$$\frac{E_f}{kT} = \frac{|S|e}{k_B} - A, \quad (21)$$

where e is the electronic charge, k_B is Boltzmann's constant and A is a dimensionless constant that depends on the scattering mechanism. $A = 1$ for amorphous materials [18, 19 same].

Fig. 10b gives the $|S|$ *versus* $1000/T$ (K^{-1}) plots. As shown, the slope $\frac{k_B}{e}\left(\frac{E_f}{kT}\right)$ is negative characterizing the non-degenerate n-type semiconductor.[59] The calculated values of $e^{E_f/kT}$ using eqn (21) are given in Table 3 for compounds **Kz1**, **Kz2**, and **Kz3** at different temperatures corresponding to the lower and higher temperature ranges, respectively.

The majority carrier (electrons) concentration N for each compound was determined using the following relation:[70]

$$N = \frac{2(2\pi m k_B T)^{3/2}}{h^3} e^{E_f/kT} \quad (22)$$

The calculated values of N at different temperatures in the relatively low and high temperature ranges for **Kz1**, **Kz2**, and **Kz3** are given in Table 3. As shown, the results of S and $e^{E_f/kT}$ for the present compounds are characteristics of non-degenerate n-type semiconductors. Table 3 and Fig. 11 summarize and compare the TE results of the present three compounds. As shown, the TE-figure of merit (zT) attained by the **Kz2** compound is the best among the other present compounds. This is due to the optimum interaction of carrier concentration, carrier mobility and molecular conformation and not only to a long π-conjugation length.

Attempts were made to improve the thermoelectric performance of the **Kz2** thin film by optimizing the carrier concentration. Annealing or exposure to an oxidizing gas (iodine doping) can respectively increase or decrease the concentration of the carrier (electrons). Annealing facilitates electron excitation (increasing carrier concentration) whereas iodine doping traps electrons (decreasing carrier concentration).

Fig. 12a shows that the carrier density, in general, increases with the increase in temperature. However, the film treatments by iodine exposure and annealing at 150 °C for 5 min have led to strong and slight declines in N values compared to its values for the pristine film, which could be mainly attributed to the trapping of electrons by iodine and the scattering increase with temperature, respectively. This change in N has similarly affected the values of all TE parameters, as seen in Fig. 12(b)–(e). Besides, elevating the annealing temperature to 200 °C has resulted in evident improvements in all TE parameters. This enhancement in PF and zT values can be attributed to the **Kz2** compound crystallinity improvement by annealing. Fig. 13 shows the X-ray diffractograms of as-deposited and annealed (200 ° C, 10 min) **Kz2** thin films, which shows the appearance of many sharp peaks after annealing. These peaks form a structural fingerprint of the compound, which implies better crystallinity. This may indicate that the thienothiophene-based compound becomes crystalline after annealing, where the C, H, and O atoms contained in the compound can be arranged together in the crystal lattice.

Besides, the relatively small value of zT of the film annealed at 200 °C for 10 min compared with its value after annealing for the shorter time of 5 min is due to the higher value of thermal conductivity caused by the longer time of annealing (Fig. 11e). This annealing effect implies that annealing is an important process in the balancing of the thermoelectric parameters (electrical conductivity, Seebeck coefficient, and thermal conductivity). The significance of the annealing is further corroborated by the summative thermoelectric outcomes in various circumstances, as given in Table 4 and Fig. 14.

Thermoelectric figure of merit (zT) was determined by using the experimentally determined electrical conductivity and Seebeck coefficient, and the thermal conductivity was determined by the Wiedemann Franz relation. It should be mentioned that in organic semiconductors, lattice vibrations are the main heat carriers, and the overall thermal conductivity is usually between 0.1 and 0.5 W m^{-1} K^{-1}. In the current research, the lattice thermal conductivity was not measured experimentally because of the limitations of the experiment, and thus, the reported zT numbers should be treated as estimated upper limits but not the exact ones. However, as the same assumptions and calculating process had been used in all samples, the comparative tendencies of thermoelectricity are still viable. The improved value of zT in **Kz2** following thermal annealing in this case is an indication of its desirable balance between electrical conductivity and Seebeck coefficient and not an exaggeration due to thermal conductivity approximation. Moreover, it is notable

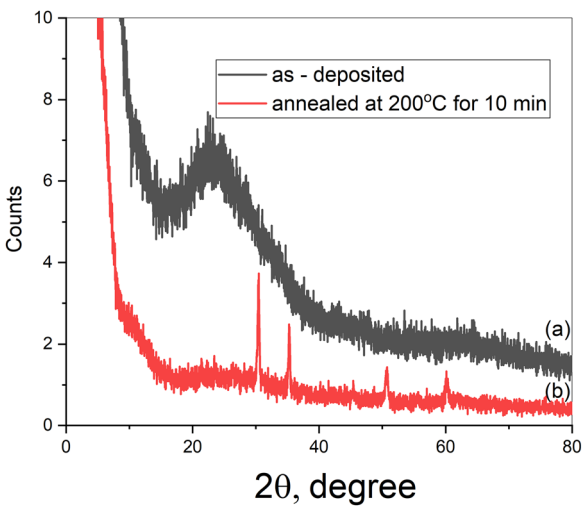

Fig. 13 X-ray diffractograms of (a) as-deposited and (b) annealed (200 °C, 10 min) **Kz2** compound thin films.

Table 4 TE parameters of **Kz2** under different conditions

Sample	T (K)	σ (Ω cm)$^{-1}$ $\times$ 10^{-4}	$-S$ (mV K^{-1})	$e^{Ef/kT}$	N, cm^{-3}	zT	PF
Kz2 (as-deposited)	493	17.2	0.85	9.73×10^{-5}	5.78×10^{17}	0.67	124
Kz2 (exposure to I_2 gas for 5 min)	493	0.92	0.43	2.56×10^{-5}	1.38×10^{15}	0.14	18
Kz2 (annealing at 150 °C for 5 min)	493	14.4	0.835	8.66×10^{-5}	4.63×10^{17}	0.65	100
Kz2 (annealing at 200 °C for 5 min)	493	31.7	3.4	0.11	3.41×10^{18}	0.78	366
Kz2 (annealing at 200 °C for 10 min)	493	36.9	3.38	0.087	2.70×10^{18}	0.77	421

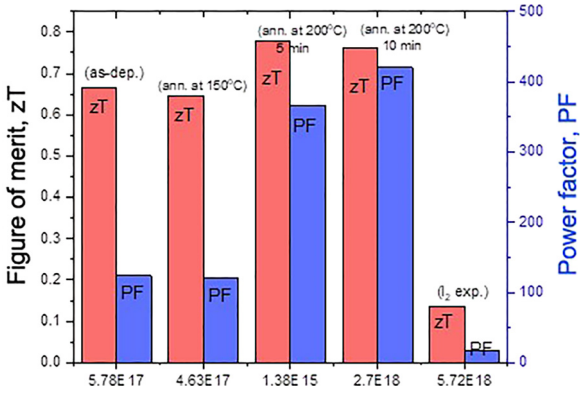

Fig. 14 Comparison of the optimal values of thermoelectric zT and PF parameters at different conditions for the thin film of **Kz2**.

that the environmental stability of the synthesized compounds during ambient conditions in the long run was not investigated in the current study. That is why, they are not device ready thermoelectric materials and these materials are proof-of-concept systems that are intended to shed light on the structure–property relations that conform to thermoelectric performance. The lattice thermal conductivity would be directly determined by the systematic evaluation of shelf-life, humidity tolerance, and thermal cycling stability, and the rational evaluation of lattice thermal conductivity would be systematically assessed.

A comparison of the optimized TE–PF and zT parameters of the **Kz2** compound with others reported for some materials is given in Table 5. It is pronounced that either PF and/or zT values of the present **Kz2** compound are better than the corresponding ones of most of the tabulated materials. However, more or less, the values of zT of the present **Kz2** organic compound can be competitive in thermoelectric applications due to its cost and scalability advantages over inorganic ones.

Summary and conclusions

Three spirothiadiazole–thienothiophene-based macroheterocyclic compounds (**Kz1–Kz3**) are synthesized under eco-friendly conditions, which are optically and electrically characterized and structurally confirmed. The spin coated thin films were found to have good uniformity, smooth surface morphology and constant thickness, which supported their high quality of optical and electrical measurements. The as-deposited films exhibit an amorphous structure and transform to a semi-crystalline structure after annealing. This structural transition from amorphous to crystalline, which is beneficial for the film's electrical and thermoelectric property improvements, is emphasized by the presence of sharp X-ray diffraction peaks for the annealed film. The films exhibit relatively high transparency in the visible and NIR regions and substantial absorption in the UV region. The optical band gaps range from 2.99 to 3.26 eV with indirect allowed transitions, which are dependent on π-conjugation. The refractive index and the extinction coefficient show typical wavelength dependent behaviour, including normal dispersion in the visible range and a steep decrease near the fundamental absorption edge, in accord with the absorption spectra of organic semiconductors. A high dielectric constant and polarizability refer to strong electronic transitions and good light–matter interaction.

Table 5 Comparison of the values of thermoelectric PF and zT parameters of the **Kz2** compound with the reported ones of some other materials

	T (K)	zT	P.F. = $S^2\sigma$ (μW m^{-1} K^{-2})	Ref.
Kz2 (as-deposited)	493	0.67	124	Present work
Kz2 (annealed at 200 °C for 5 min)	493	0.78	366	
Kz2 (annealed at 200 °C for 10 min)	493	0.77	421	
Type (I)-p ($Bi_{0.5}Sb_{1.5}Te_3$)	373	1.3	34	70
Type (II)-p ($Bi_{0.4}Sb_{1.6}Te_3$)	373	1.25	47	70
p-PbTe(Mg,Na)	800	1.67	24.1	71
Tetrakis(dimethylamino)ethylene	400	0.5	1040	72
Ethylene glycol-mixed PEDOT:PSS	300	0.28	350	73
Poly[Na_x(Ni-1,1,2,2-ethenetetrathiolate)s]	440	0.1	27.62	74
PEDOT:PSS/SWCNT TE thin films	350	0.43	501.31 $\pm$ 19.23	75
PEDOT:PSS TE fibers	300	0.27	147.8	76
Mixing of RN120-SWCNTs with P1. RN120-SWCNT (G2)	300	—	96.8	77
Polymer poly(benzodifurandione) benzodipyrandione (BPDO) (PBFDO)	400	0.25	142	78

Overall, the results indicate the potential of the synthesized materials for use in optoelectronic and photonic devices. Seebeck coefficients with negative values verify electrons as the major charge carriers. The electrical conductivity steadily increased with the temperature, reflecting the typical thermally activated transport characteristic of organic semiconductors. Among the evaluated materials, the **Kz2** compound exhibited the most promising thermoelectric performance with a power factor of 366 μW m^{-1} K^{-2} and a zT of 0.78 at 493 K after 5-minute annealing treatment of 200 °C. This is performance that can be attributed to two factors. First, the coil conformation of **Kz2** where the coil is linearly expanded, provides a more efficient method of transporting charge carriers as compared to a compact or folded coil conformation. Second, annealing increases the concentration of carriers as well as crystallinity of the material, which further improves thermoelectric activity. On the whole, the findings have defined a direct relation between the molecular structure, conjugation, conformation, and thermoelectric performance, indicating that spirothiadiazole–thienothiophene macroheterocycles are potential candidates for use as multifunctional organic materials in flexible energy harvesting and optoelectronic technology.

Conflicts of interest

The authors declare that they have no known competing financial interests or personal relationships that could have appeared to influence the work reported in this paper.

Data availability

The authors declare that the data supporting the findings of this study are available within the supplementary information (SI). Supplementary information is available. See DOI: https://doi.org/10.1039/d6ma00174b.

Acknowledgements

The authors gratefully acknowledge the support provided by Sohag University, Sohag, Egypt, for facilitating the synthesis, characterization, and research facilities used in this study.

References

1 A. Facchetti, π-Conjugated polymers for organic electronics and photovoltaic cell applications, *Chem. Mater.*, 2011, **23**(3), 733–758.
2 C. Liu, L. Shao, S. Chen, Z. Hu, H. Cai and F. Huang, Recent progress in π-conjugated polymers for organic photovoltaics: solar cells and photodetectors, *Prog. Polym. Sci.*, 2023, **143**, 101711.
3 S. R. Forrest, The path to ubiquitous and low-cost organic electronic appliances on plastic, *Nature*, 2004, **428**(6986), 911–918.
4 H. M. Abd El-Lateef, M. S. Kamel, M. M. Khalaf and M. A. E. A. A. Ali, Studying the effect of annealing temperature on the optical characteristics of conjugated pyrrolo[2,3-*b*] pyrrole azo dye thin films for optoelectronic devices, *Opt. Mater.*, 2024, **157**, 116343.
5 H. M. Abd El-Lateef, M. S. Kamel, A. Y. A. Alzahrani, M. M. Khalaf, M. Gouda and M. A. E. A. A. Ali, Synthesis, characterization, and study of linear and non-linear optical properties of some newly thieno [2,3-*b*] thiophene analogs, *Semicond. Sci. Technol.*, 2024, **39**(12), 125014.
6 C. Bizzarri, E. Spuling, D. M. Knoll, D. Volz and S. Bräse, Sustainable metal complexes for organic light-emitting diodes (OLEDs), *Coord. Chem. Rev.*, 2018, **373**, 49–82.
7 P. G. V. Sampaio and M. O. A. González, A review on organic photovoltaic cell, *Int. J. Energy Res.*, 2022, **46**(13), 17813–17828.
8 H. Sirringhaus, Device physics of solution-processed organic field-effect transistors, *Adv. Mater.*, 2005, **17**(20), 2411–2425.
9 Y. Liu, J. Zhao, Z. Li, C. Mu, W. Ma, H. Hu, K. Jiang, H. Lin, H. Ade and H. Yan, Aggregation and morphology control enables multiple cases of high-efficiency polymer solar cells, *Nat. Commun.*, 2014, **5**(1), 5293.
10 A. M. Soliman, M. Abd El Aleem Ali Ali El-Remail, M. S. Kamel, A. El-Araby and E. K. Shokr, Synthesis, optical linear and non-linear characterization and metal ion sensing application of some novel thieno [2,3-*b*] thiophene-2, 5-dicarbohydrazide Schiff base derivatives, *Sci. Rep.*, 2025, **15**(1), 1611.
11 Z. S. Zhang, L. Ye and J. Hou, Breaking the 10% efficiency barrier in organic photovoltaics: Morphology and device optimization of well-known PBDTTT polymers, *Adv. Energy Mater.*, 2016, **6**(11), 1502529.
12 E. K. Shokr, M. A. E. Ali, M. S. Kamel, A. El-Araby and A. M. Soliman, Optoelectronic characterizations, and RT-NH3 gas sensing application of newly synthesized spiro [indoline-3, 4′-pyrano [2,3-*b*] pyridine] derivative, *Mater. Sci. Semicond. Process.*, 2025, **188**, 109201.
13 E. K. Shokr, M. S. Kamel, H. Abdel-Ghany, M. A. E. A. Ali and A. Abdou, Synthesis, characterization, and DFT study of linear and non-linear optical properties of some novel thieno [2,3-*b*] thiophene azo dye derivatives, *Mater. Chem. Phys.*, 2022, **290**, 126646.
14 M. O. Aboelez, M. A. E. A. Ali, M. S. Kamel, W. A. Fadaly, M. T. Nemr and H. A. Ezelarab, Novel 3, 4-diaminothieno [2,3-*b*] thiophene-2, 5-dicarbohydrazide-based scaffolds as EGFRWT, EGFRT790M, and tubulin polymerization inhibitors with anti-proliferative activity, *Bioorg. Chem.*, 2025, 108728.
15 Y. Wu and W. Zhu, Organic sensitizers from D–π–A to D–A–π–A: effect of the internal electron-withdrawing units on molecular absorption, energy levels and photovoltaic performances, *Chem. Soc. Rev.*, 2013, **42**(5), 2039–2058.
16 L. Jia and Y. Liu, The effects of electron-withdrawing and electron-donating groups on the photophysical properties and ESIPT of salicylideneaniline, *Spectrochim. Acta, Part A*, 2020, **242**, 118719.

17 T. Sutradhar and A. Misra, Role of electron-donating and electron-withdrawing groups in tuning the optoelectronic properties of difluoroboron–napthyridine analogues, *J. Phys. Chem. A*, 2018, **122**(16), 4111–4120.
18 Z. Hu, B. Shao, G. T. Geberth and D. A. Vanden Bout, Effects of molecular architecture on morphology and photophysics in conjugated polymers: from single molecules to bulk, *Chem. Sci.*, 2018, **9**(5), 1101–1111.
19 B. J. Schwartz, Conjugated polymers as molecular materials: How chain conformation and film morphology influence energy transfer and interchain interactions, *Annu. Rev. Phys. Chem.*, 2003, **54**(1), 141–172.
20 Y. Zhou, K. Zhang, Z. Chen and H. Zhang, Molecular design concept for enhancement charge carrier mobility in OFETs: a review, *Materials*, 2023, **16**(20), 6645.
21 H. F. Haneef, A. M. Zeidell and O. D. Jurchescu, Charge carrier traps in organic semiconductors: a review on the underlying physics and impact on electronic devices, *J. Mater. Chem. C*, 2020, **8**(3), 759–787.
22 A. El-Shafei, A. El-Saghier and E. Ahmed, Synthesis of some new spiro (pyran-4, 2′-benzoxazole) derivatives, *Synthesis*, 1994, (02), 152–154.
23 M. A. Mohamed, A. M. Kadry, S. A. Bekhit, M. A. Abourehab, K. Amagase, T. M. Ibrahim, A. M. El-Saghier and A. A. Bekhit, Spiro heterocycles bearing piperidine moiety as potential scaffold for antileishmanial activity: synthesis, biological evaluation, and in silico studies, *J. Enzyme Inhib. Med. Chem.*, 2023, **38**(1), 330–342.
24 A. H. Abdelmonsef, A. M. El-Saghier and A. M. Kadry, Ultrasound-assisted green synthesis of triazole-based azomethine/thiazolidin-4-one hybrid inhibitors for cancer therapy through targeting dysregulation signatures of some Rab proteins, *Green Chem. Lett. Rev.*, 2023, **16**(1), 2150394.
25 Y. N. Nayak, S. L. Gaonkar and M. Sabu, Chalcones: Versatile intermediates in heterocyclic synthesis, *J. Heterocycl. Chem.*, 2023, **60(8)**, 1301.
26 M. A. Mohamed, A. M. Kadry, M. M. Farghaly and M. M. El-Saghier, Synthesis, characterization and antibacterial activity of some novel spiro [naphtho [1, 2-*e*][1, 3] oxazine-3, 4′-pyran] derivatives, *J. Heterocycl. Chem.*, 2021, **7**(3), 1–10.
27 P. Setif, S. Acker, B. Lagoutte and J. Duranton, Contribution to the structural characterization of eucaryotic PSI reaction centre—II. Characterization of a highly purified photoactive SDS-CP1 complex, *Photosynth. Res.*, 1980, **1**, 17–27.
28 E. K. Shokr, S. A. Elkot, M. S. Kamel and H. Ali, Highly efficient (V2O5) 0.91 Zn0. 09 powdered catalyst for water organic pollutant elimination, *Optik*, 2024, **302**, 171718.
29 J. R. S. Jassas, O. A. Omran, A. Abdou, M. S. Kamel, Z. Moussa, A. Abd-El-Aziz, N. Ma, H. M. Altass, A. S. Khder and E. M. Hussein, Design and DFT calculations of optoelectronic material based on thiazolobenzimidazole-coupled isatin derivatives, *Mater. Chem. Phys.*, 2024, **325**, 129689.
30 E. K. Shokr, H. Ali, H. A. Mohamed, M. S. Kamel and H. Mohamed, Optical characterization of MoS2 and MoS2/Zn synthesized by thermal evaporation and sol-gel spin-coating techniques for gas-sensing and NLO-applications, *Phys. B*, 2024, **683**, 415936.
31 E. K. Shokr, H. A. Mohamed, H. Mohamed, M. S. Kamel and H. Ali, Enhancing the MoS2/MoO3/ZnS/Zn-Heterojunction catalyst's photocatalytic performance for water organic pollutants, *Phys. Scr.*, 2023, **98**(8), 085917.
32 J. Roncali, Molecular bulk heterojunctions: an emerging approach to organic solar cells, *Acc. Chem. Res.*, 2009, **42**(11), 1719–1730.
33 M. Fox, *Optical properties of solids*, Oxford University Press, 2010, vol. 3.
34 F. Urbach, The long-wavelength edge of photographic sensitivity and of the electronic absorption of solids, *Phys. Rev.*, 1953, **92**(5), 1324.
35 M. Sharaf, A. H. Moustafa, M. A. Mohamed, M. S. Kamel, A. Abdou and O. A. Omran, Stereoselective synthesis, optical characterization, DFT, and metal ion detection of tetra p-tert-butylthiacalix [4] arene derivatives containing amide and thiamide fragments at lower rim, *Tetrahedron Lett.*, 2025, **168**, 155709.
36 M. Sharaf, A. H. Moustafa, M. A. Mohamed, M. S. Kamel, A. Abdou and O. A. Omran, Optimized design and optical evaluation of mono-chalcone thiacalix [4] arene thin films for UV-blocking and nonlinear photonic applications, *J. Mol. Struct.*, 2025, 144102.
37 T. Moss, A relationship between the refractive index and the infra-red threshold of sensitivity for photoconductors, *J. Chem. Soc.*, 1950, **63**(3), 167.
38 M. A. E. A. A. Ali, M. S. Kamel, S. A. Halim, E. K. Shokr, H. Abdel-Ghany and H. Hamad, Facile synthesis and photodetection characteristics of new pyrrolo [2,3-*b*] pyrrole-based metal-free organic dyes containing phenols as the potential candidates towards energy conversion, *Mater. Chem. Phys.*, 2023, **293**, 126972.
39 J. Tauc, R. Grigorovici and A. Vancu, Optical properties and electronic structure of amorphous germanium, *Phys. Status Solidi B*, 1966, **15**(2), 627–637.
40 E. K. Shokr, Optimization of the electrical and optical properties of Sb-Sn-O thin films, *Semicond. Sci. Technol.*, 2000, **15**(3), 247.
41 M. S. Kamel, A. M. Abu Dief, M. A. E. A. A. A. El Remaily, K. A. Abu Al-Ola, A. Y. A. Alzahrani, M. H. AL Mughram and T. N. A. Eskander, Fabrication, Structural Elucidation, and Optical Linear and Nonlinear Characteristics of Ruthenium (III) and Chromium (III) Chelates Generated From Benzylidene-Amino-Phenyl-Phenyl-Methanone Ligand, *ChemistrySelect*, 2025, **10**(36), e02209.
42 E. K. Shokr, S. A. Elkot, M. S. Kamel and H. Ali, Sol-gel spin-coated V2O3 thin films for Optical HCl and Iodine gas sensing, *Opt. Mater.*, 2024, **151**, 115263.
43 A. Mindil, M. S. Kamel, M. Mohery, E. A. Al-Harthi, E. K. Shokr and A. Y. Moustafa, Indium-doped melanin efficient photocatalyst for water purification from organic pollutants, *Phys. Scr.*, 2025, **100**(9), 095523.
44 M. B. Hawsawi, O. A. Omran, A. Abdou, M. S. Kamel, A. M. Almohyawi, M. S. Alluhaibi, R. I. Alsantali,

Z. Moussa, A. Timoumi and E. M. Hussein, High nonlinear optical performance of p-tert-butylthiacalix [4] arene derivatives: Synthesis, characterization, and theoretical validation, *Opt. Mater.*, 2025, **160**, 116642.

45 S. Mahjabin, M. M. Haque, S. Khan, V. Selvanathan, M. Jamal, M. Bashar, H. I. Alkhammash, M. I. Hossain, M. Shahiduzzaman and N. Amin, Effects of oxygen concentration variation on the structural and optical properties of reactive sputtered WOx thin film, *Sol. Energy*, 2021, **222**, 202–211.

46 K. Sharma, A. S. Al-Kabbi, G. Saini and S. Tripathi, Determination of dispersive optical constants of nanocrystalline CdSe (nc-CdSe) thin films, *Mater. Res. Bull.*, 2012, **47**(6), 1400–1406.

47 A. Ait Hssi, L. Atourki, N. Labchir, M. Ouafi, K. Abouabassi, A. Elfanaoui, A. Ihlal and K. Bouabid, Optical and dielectric properties of electrochemically deposited p-Cu2O films, *Mater. Res. Express*, 2020, **7**(1), 016424.

48 T. Ghosh, S. K. Sharma and D. Pradhan, Giant Dielectric Constant and Superior Photovoltaic Property of the Mechanochemically Synthesized Stable CH3NH3PbBr3 in a Hole Transporter-Free Solar Cell, *ACS Sustainable Chem. Eng.*, 2019, **8**(3), 1445–1454.

49 W. Steinmann, Optical plasma resonances in solids, *Phys. Status Solidi B*, 1968, **28**(2), 437–462.

50 S. H. Wemple and M. DiDomenico Jr, Behavior of the electronic dielectric constant in covalent and ionic materials, *Phys. Rev. B*, 1971, **3**(4), 1338.

51 E. K. Shokr, M. S. Kamel, H. Abdel-Ghany and M. A. E. A. A. Ali, Optical characterization and effects of iodine vapor & gaseous HCl adsorption investigation of novel synthesized organic dye based on thieno [2,3-*b*] thiophene, *Optik*, 2021, **243**, 167385.

52 J. Tyczkowski and R. Ledzion, Electronic band structure of insulating hydrogenated carbon-germanium films, *J. Appl. Phys.*, 1999, **86**(8), 4412–4418.

53 S. M. Abdelhamid, M. Dongol, A. Elhady and A. A. Abuelwafa, Role of vacuum annealing on the structural, optical properties and Dc conductivity of titanium (IV) phthalocyanine dichloride thin films, *Phys. Scr.*, 2023, **98**(12), 125960.

54 A. A. Abuelwafa, S. Elnobi, M. A. Santos and H. M. Alsoghier, A novel organic semiconductor 4-phenylthiazol-2-yl-(phenylhydrazono) acetonitrile (PTPA) thin films: synthesis, optical and electrical properties, *Sci. Rep.*, 2023, **13**(1), 12973.

55 S. I. Qashou, A. Darwish and S. Al Garni, Enhancement of microstructure and electrical conductivity of N,N′-dimethyl-3, 4, 9, 10-perylenedicarboximide nanostructured films by thermal annealing for photoelectronic applications, *Synth. Met.*, 2018, **242**, 67–72.

56 M. El-Nahass, H. Zeyada, K. Abd-El-Rahman and A. A. Darwish, Structural characterization and electrical properties of nanostructured 4-tricyanovinyl-N, N-diethylaniline thin films, *Eur. Phys. J.:Appl. Phys.*, 2013, **62**(1), 10202.

57 G. Chester and A. Thellung, Mott's formula for the thermopower and the Wiedemann-Franz law, *Phys. Rev. B:Condens. Matter Mater. Phys.*, 1980, **21**(10), 4223.

58 G. Chester and A. Thellung, The law of Wiedemann and Franz, *Proc. Phys. Soc.*, 1961, **77**(5), 1005.

59 M. Ibrahim, M. Wakkad and E. K. Shokr, Conduction mechanisms of antimony selenide, *J. Therm. Anal. Calorim.*, 1994, **42**(6), 1193–1205.

60 M. Ibrahim, M. Wakkad, E. K. Shokr and H. Abd El-Ghani, Electrical properties of antimony telluride, *Appl. Phys. A:Solids Surf.*, 1991, **52**(4), 237–241.

61 E. K. Shokr, Optical properties of glassy Ge20Te80-xSex thin films, *Indian J. Pure Appl. Phys.*, 1992, **30**(6), 271–275.

62 Q. Wei, M. Mukaida, K. Kirihara, Y. Naitoh and T. Ishida, Recent progress on PEDOT-based thermoelectric materials, *Materials*, 2015, **8**(2), 732–750.

63 J. Ouyang, Q. Xu, C.-W. Chu, Y. Yang, G. Li and J. Shinar, On the mechanism of conductivity enhancement in poly (3, 4-ethylenedioxythiophene): poly (styrene sulfonate) film through solvent treatment, *Polymer*, 2004, **45**(25), 8443–8450.

64 Z. Liang, Y. Zhang, M. Souri, X. Luo, A. M. Boehm, R. Li, Y. Zhang, T. Wang, D.-Y. Kim and J. Mei, Influence of dopant size and electron affinity on the electrical conductivity and thermoelectric properties of a series of conjugated polymers, *J. Mater. Chem. A*, 2018, **6**(34), 16495–16505.

65 H. Lee, S. B. Lee, Y.-S. Kim, H. Kim, M.-J. Kim, T. W. Yoon, D. Lee, J. H. Cho, Y.-H. Kim and B. Kang, Boosting thermoelectric performance of conjugated polymers via interchain molecular docking: Significance of highly crystalline and percolated morphology, *Chem. Eng. J.*, 2023, **468**, 143654.

66 E. Isotta, B. Mukherjee, C. Fanciulli, N. Ataollahi, I. Sergueev, S. Stankov, R. Edla, N. M. Pugno and P. Scardi, Origin of a simultaneous suppression of thermal conductivity and increase of electrical conductivity and seebeck coefficient in disordered cubic Cu2ZnSnS4, *Phys. Rev. Appl.*, 2020, **14**(6), 064073.

67 N. F. Mott and E. A. Davis, *Electronic processes in non-crystalline materials*, OUP, Oxford, 2012.

68 N. K. Hindley, Random phase model of amorphous semiconductors I. Transport and optical properties, *J. Non-Cryst. Solids*, 1970, **5**(1), 17–30.

69 F. Benko and F. Koffyberg, Quantum efficiency and optical transitions of CdO photoanodes, *Solid State Commun.*, 1986, **57**(12), 901–903.

70 A. Nozariasbmarz, B. Poudel, W. Li, H. B. Kang, H. Zhu and S. Priya, Bismuth telluride thermoelectrics with 8% module efficiency for waste heat recovery application, *iScience*, 2020, **23**(7), 101340.

71 F. Benko and F. Koffyberg, Figure of merit ZT of a thermoelectric device defined from materials properties, *Energy Environ. Sci.*, 2017, **10**(11), 2280–2283.

72 H. Wang, J. H. Hsu, S. I. Yi, S. L. Kim, K. Choi, G. Yang and C. Yu, Thermally driven large n-type voltage responses from hybrids of carbon nanotubes and poly (3, 4-ethylenedioxythiophene) with tetrakis (dimethylamino) ethylene, *Adv. Mater.*, 2015, **27**(43), 6855–6861.

73 G.-H. Kim, L. Shao, K. Zhang and K. P. Pipe, Engineered doping of organic semiconductors for enhanced thermoelectric efficiency, *Nat. Mater.*, 2013, **12**(8), 719–723.

74 Y. Sun, P. Sheng, C. Di, F. Jiao, W. Xu, D. Qiu and D. Zhu, Organic thermoelectric materials and devices based on p-and n-type poly (metal 1, 1, 2, 2-ethenetetrathiolate) s, *Adv. Mater.*, 2012, **24**(7), 932–937.

75 M. Zhang, X. Cao, M. Wen, C. Chen, Q. Wen, Q. Fu and H. Deng, Highly electrical conductive PEDOT: PSS/SWCNT flexible thermoelectric films fabricated by a high-velocity non-solvent turbulent secondary doping approach, *ACS Appl. Mater. Interfaces*, 2023, **15**(8), 10947–10957.

76 N. Wen, Z. Fan, S. Yang, Y. Zhao, T. Cong, S. Xu, H. Zhang, J. Wang, H. Huang and C. Li, Highly conductive, ultra-flexible and continuously processable PEDOT: PSS fibers with high thermoelectric properties for wearable energy harvesting, *Nano Energy*, 2020, **78**, 105361.

77 M. Idir, G. Chamelot, Y. He, T. Lemieux, K. Bueley, S. Beaupré, S. Alem, J. Lu, J.-F. Morin and M. Leclerc, Organic thermoelectric films: achieving high conductivity and power factor through sulfonated-poly (3, 4-ethylene-dioxythiophene) and single-walled carbon nanotube composites, *J. Mater. Chem. C*, 2026, **14**, 2854–2861.

78 H. Ji, J. G. Lee, H. Lee, D. Kim and K. Cho, High-performance organic thermoelectric materials based on n-type conjugated polymers via chemical isomerization-induced charge transport modulation, *Mater. Horiz.*, 2025, **12**(21), 9250–9261.